A thermomechanical numerical model for crustal accretion of medium to fast spreading mid-ocean ridges

Philippe Machetel, C. J. Garrido

Geochemistry Geophysics Geosystems G3
AN ELECTRONIC JOURNAL OF THE EARTH SCIENCES
Published by AGU and the Geochemical Society

Article
Volume 10, Number 3
12 March 2009
Q03008, doi:10.1029/2008GC002270
ISSN: 1525-2027

A thermomechanical numerical model for crustal accretion of medium to fast spreading mid-ocean ridges

P. Machetel
Geosciences Montpellier, UMR5243, CNRS, UM2, Place Eugène Bataillon, F-34090 Montpellier CEDEX, France (philippe.machetel@laposte.net)

C. J. Garrido
Instituto Andaluz de Ciencias de la Tierra, CSIC-UGR, Facultad de Ciencias, Fuentenueva S/N, E-18001 Granada, Spain (carlosg@ugr.es)

[1] We propose a new thermomechanical numerical model of mid-ocean ridge accretion aimed at investigating asymmetric spreading rates, diverse configurations of lens and sill magma injections, crystallization and depth, and on- and off-axis patterns of hydrothermal cooling. The numerical algorithm iteratively resolves temperature and motion equations until it reaches a stationary solution. The motion equation was written in a vorticity-stream function formalism, with boundary and internal conditions applied to the stream function to impose the style of magma injection. Unlike in previous models, our model does not assume an a priori shape for the temperature field, which is initiated by an initial half-space cooling according to the left and right spreading rates. Complex patterns of hydrothermal cooling are simulated by enhanced thermal diffusivity. The model succeeds in describing the dynamic and thermal effects of spreading rates, the style of magma intrusion, and the hydrothermal cooling. Accurate descriptions of these are essential to study the cooling histories of crustal rocks and geophysical observables.

Components: 3954 words, 5 figures, 1 table.

Keywords: mid-oceanic ridge; numerical models; asymmetric ridge; hydrothermal cooling; magma chamber; cooling history.

Index Terms: 1032 Geochemistry: Mid-oceanic ridge processes (3614, 8416); 1036 Geochemistry: Magma chamber processes (3618); 0545 Computational Geophysics: Modeling (4255).

Received 3 March 2008; **Revised** 6 October 2008; **Accepted** 10 November 2008; **Published** 12 March 2009.

Machetel, P., and C. J. Garrido (2009), A thermomechanical numerical model for crustal accretion of medium to fast spreading mid-ocean ridges, *Geochem. Geophys. Geosyst.*, *10*, Q03008, doi:10.1029/2008GC002270.

1. Introduction

[2] Since the discovery of steady state magma chambers in fast to medium spreading mid-ocean ridges, numerical models of lower oceanic crust generation have become increasingly sophisticated to reproduce geophysical observations from active spreading ridges as well as field and petrological observations from ophiolites. Proposed numerical models of the oceanic crust can be classified into two main categories: thermal models [*Maclennan et al.*, 2004; *Morton and Sleep*, 1985; *Sleep*, 1975] and thermomechanical models [*Chen and Phipps Morgan*, 1996; *Chen*, 2001; *Chenevez et al.*, 1998; *Phipps Morgan*

and Chen, 1993]. In accordance with available geophysical observations, earlier thermal models of the oceanic crust investigated crustal accretion in a single, perched melt lens below the sheeted dikes and incorporated hydrothermal heat removal by means of heat sinks [*Morton and Sleep*, 1985]. These works were soon followed by thermomechanical models of passive crustal flow that explored igneous accretion in a single melt lens and in-axis heat removal by hydrothermal cooling simulated through variable thermal conductivity [*Phipps Morgan and Chen*, 1993].

[3] With the advent of geophysical and field evidence pointing to the accretion of oceanic crust in multiple on-axis melt injections [*Boudier and Nicolas*, 1995; *Boudier et al.*, 1996; *Garmany*, 1989; *Kelemen et al.*, 1997], numerical models of oceanic crust have investigated the thermal and flow consequences of variable melt injection geometries. *Chenevez et al.* [1998] proposed fully dynamic, thermomechanical models of active crustal flow that included a second deeper melt lens above the Moho. These authors also considered viscosity transitions due to crystallization and convection in the mush zone. Their model not only constrained the minimum viscosity of the magma chamber to prevent convection but also demonstrated that a weak variation between the thermal diffusivity end-members of the hot and cold parts of the crust made the injection of melt at the Moho thermally viable. In order to assess the thermal effects of gabbro accretion from the lower melt lens, *Chen* [2001] developed a thermomechanical model of passive crustal flow that includes a second deeper melt lens above the Moho. He concluded that, if a significant (>10%) amount of gabbro crystallized near the Moho, the latent heat released during crystallization would generate a large "molten" section of the lower crust due to the inability of cold seawater to penetrate into this hot region. This makes accretion models proposing multiple injections at the ridge axis thermally infeasible. As further geophysical data and compliance measurements along the EPR seem to confirm that on-axis melt lenses may also be present at Moho depths [*Crawford and Webb*, 2002; *Dunn et al.*, 2000; *Nedimovic et al.*, 2005], much focus has shifted to the effectiveness of near, off-axis cooling for extracting the heat of crystallization from the deep crust. The effectiveness and extent of off-axis cooling is a key issue for the feasibility of oceanic crust models proposing multiple injections in the lower crust [*Coogan et al.*, 2002; *Coogan et al.*, 2007; *Garrido et al.*, 2001].

[4] *Cherkaoui et al.* [2003] explicitly included fluid flow in the crust below a given temperature, and although they treated crystallization and crustal accretion simply, they showed the feasibility of deep, near off-axis hydrothermal cooling. Recently, more sophisticated thermal models have included petrological variations and variable distributions of melt within the magma chamber [*Maclennan et al.*, 2004; 2005]. While these thermal models reproduce the broad geophysical observations from active ridges, a number of outstanding questions remain regarding ad hoc flow patterns of the oceanic crust for different models. The feedbacks between cooling, viscosity, and the style of magma injections modify the final flow pattern that changes the thermal and cooling histories of the oceanic crust. Neither thermal nor thermomechanical models have taken into account the existence of asymmetric spreading rate ridges, as in the central part of the Mariana Basin [*Deschamps and Fujiwara*, 2003]. As of yet, owing to the complexity of simulating crustal flow with multiple injections at the ridge axis and the effects of variable in- and off-axis hydrothermal cooling, there are no available thermomechanical models. In this paper, we report a new numerical model aiming to simulate ridge dynamics by focusing on three physical processes: (1) the symmetry of the ridge spreading; (2) the style of magma intrusions (through perched lens and/or axial sill intrusions); and (3) the effects of deep and off-axis hydrothermal cooling.

2. General Philosophy

[5] We have built this code to let the mass, momentum, and thermal energy conservation equations shape the thermal and dynamic structures of the solution within a fluid mechanic theoretical framework. Thus, a priori assumptions do not condition the flow pattern of the magma chamber, which results from the interactions of the thermal and mechanical effects of the left and right spreading rates, the style of magma injection (through a perched lens and/or sills), and the locally enhanced thermal conductivity that simulates hydrothermal cooling. In nature, magma crystallization leads to latent heat release and abrupt viscosity jumps over a narrow range of temperature. These viscosity variations affect the pattern of crustal flow that modifies temperature through heat advection. The only way to investigate the coupling between

asymmetric spreading rates, styles of magma intrusions, and hydrothermal cooling requires iteratively solving both the motion and the temperature equations.

3. Conservation Equations

[6] The basic conservation equations of the model are similar to those of previous thermomechanical models [*Chenevez et al.*, 1998]. The first depicts mass conservation for an incompressible fluid in a two-dimensional plane (equation (1)). This geometrical condition is verified for medium to fast spreading ridges for which the crustal motion is mainly perpendicular to the ridge axis (see Table 1 for notations).

$$\frac{\partial v_x}{\partial x}+\frac{\partial v_y}{\partial y}=0 \tag{1}$$

The existence of this zero-divergence velocity field enables us to derive the fluid velocity components from a stream function ψ (equation (2)).

$$v_x=\frac{\partial \psi}{\partial y};\quad v_y=-\frac{\partial \psi}{\partial x}. \tag{2}$$

Then, the equation of momentum conservation (simplified for the infinite Prandtl number approximation) reduces to the classical Navier-Stockes equation (equation (3)), which describes the equilibrium between the body forces, including gravity, the pressure gradient and the divergence of the stress tensor.

$$\rho\ \mathbf{g}+\nabla.\tau-\nabla p=0 \tag{3}$$

$$\tau=\eta\left(\nabla\vec{v}+\nabla\vec{v}^{T}\right) \tag{4}$$

Within a 2-D framework, the vorticity vector, $\boldsymbol{\omega} = \nabla \times \mathbf{v}$, has only one nonzero component, ω, parallel to the ridge axis. This property allows us to rewrite the continuity and momentum equations using, for ψ and ω, two Laplacians. This has been done keeping all the nonconstant terms for the first and second order spatial viscosity derivatives (equations (5) and (6)).

$$\nabla^2\ \psi+\omega=0 \tag{5}$$

$$\nabla^2(\eta\ \omega)=-4\frac{\partial^2\psi}{\partial x\partial y}\frac{\partial^2\eta}{\partial x\partial y}-2\frac{\partial^2\psi}{\partial x^2}\frac{\partial^2\eta}{\partial y^2}-2\frac{\partial^2\psi}{\partial y^2}\frac{\partial^2\eta}{\partial x^2} \tag{6}$$

Finally, the conservation of energy equation has been written using its temperature formulation (equation (7)), in which all the nonconstant terms for thermal conductivity, viscous heating, and crystallization latent heat release have also been kept.

$$\rho\ C_p\ \frac{d(T)}{dt}=\mathrm{div}\ k\ \mathrm{grad}T+\rho\ Q_L\ \frac{d\Gamma_c}{dt}+\tau_{ik}\ \frac{\partial v_i}{\partial x_k} \tag{7}$$

4. External Boundary Conditions

[7] Figure 1 summarizes the boundary and initial conditions required to compute motion (Figure 1, top) and temperature (Figure 1, bottom). The Ψ difference between two points of the computation area measures a lineic discharge by meter of the ridge axis (in m^2/s). Thus, the Ψ jump at the bottom ridge axis (magma injection) is also equal to the total crust lineic discharge of the ridge, Ψ_c, and to the lineic flow of matter escaping through both sides of the ridges (equation (8)).

$$\psi_c=\left(v_{pl}+v_{pr}\right)H \tag{8}$$

From this basic mass conservation condition, it is possible to express the boundary conditions around the computation box in term of Ψ_c according to equations (9) through (13).

$$\psi_{bl}=\frac{\psi_c}{2} \tag{9}$$

$$\psi_l(y)=\frac{\psi_c}{2}-V_{pl}\ y \tag{10}$$

$$\psi_t=\frac{\psi_c}{2}-V_{pl}\ H \tag{11}$$

$$\psi_r(y)=\frac{\psi_c}{2}-V_{pl}\ H-V_{pr}(H-y) \tag{12}$$

$$\psi_{br}=\frac{\psi_c}{2}-V_{pl}\ H-V_{pr}\ H \tag{13}$$

As emphasized by previous works [*Chenevez et al.*, 1998], the choice of boundary temperature may influence the structure of the final stationary thermal field through the computation process. To avoid this a priori, our model only assumes a constant seafloor temperature (0°C) and conductive gradients from the half-infinite cooling law that are reached at the lateral edges of the computation box

Table 1. Notations and Values Used in This Paper

Notations	Name (Units)	Typical Value
Fluid velocity	v (m/s)	
Horizontal coordinate (offset from ridge)	x (m)	−L to L
Vertical coordinate (height above Moho)	y (m)	0 to H
Vertical coordinate (depth below seafloor)	z (m)	0 to H
Temperature	T (°C)	
Pressure	p (N/m^2)	
Strain	τ (N/m^2)	
Stream function	ψ (m^2/s)	
Vorticity	ω (s^{-1})	
Time	t (s)	
Density	ρ (kg/m^3)	
Thermal conductivity	k (J/(m s K))	
Dynamic viscosity	η (Pa.s)	
Heat capacity by unit of mass	Cp (J/kg K)	
Latent heat of crystallization	Q_L (J/kg)	500×10^3
Gravity acceleration	g (m/s^2)	
Crystallization function	Γ_c (−)	0 to 1
Medium crystallization temperature	T_c (°C)	1230
Crystallization temperature interval	δT (°C)	60
Hydrothermal cooling horizontal function	Γ_o (−)	0 to 1
Distance for off-axis hydrothermal cooling	x_o (m)	10,000
Interval for off-axis hydrothermal cooling	δ x_o (m)	10,000
Hydrothermal cooling vertical function	Γ_d (−)	0 to 1
Depth for hydrothermal cooling	y_c (m)	2250
Depth interval for off hydrothermal cooling	δ y_c (m)	200
Weak viscosity (weak phase)	η_w (Pa.s)	5×10^{14}
Strong viscosity (strong phase)	η_s (Pa.s)	5×10^{15}
High thermal conductivity	k_h(J/(m s K))	5 or 25.
Low thermal conductivity	k_l(J/(m s K))	2.5
Thickness from Moho to seafloor	H (m)	6000
Distance from ridge to lateral box boundary	L (m)	20,000
Left plate velocity	V_{pl} (m/s)	
Right plate velocity	V_{pr} (m/s)	
Lens height above Moho	y_l (m)	
Total lineic ridge discharge	ψ_c (m^2/s)	
Stream function bottom left boundary	ψ_{bl} (m^2/s)	
Stream function lateral left boundary	ψ_l (m^2/s)	
Stream function top boundary	ψ_t (m^2/s)	
Stream function lateral right boundary	ψ_r (m^2/s)	
Stream function bottom right boundary	ψ_{br} (m^2/s)	
Intensity of injection through the lens	I_l (−)	0 to 1
Number of left sills	n_{ls}	
Intensity of injection through the left sill n	I_{sln} (−)	<1
Number of right sills	n_{rs}	
Intensity of injection through the right sill	I_{srn} (−)	<1
Seafloor temperature	T_s(°C)	0
Intrusion temperature	T_i(°C)	1280
Number of horizontal grid points	Nx	600 or 1798
Number of vertical grid points	Ny	100 or 298

according to the left and right spreading rates (V_p = V_{pl} or V_{pr} in equation (14)) (Figure 1, bottom).

$$T(x,y) = (T_{mi} - 273)erf\left(\frac{z}{2}\sqrt{\frac{\rho\ C_p\ V_p}{k_m|x|}}\right) + 273 \qquad (14)$$

Free slip conditions are applied for vorticity around the box boundaries (ω = 0).

5. Simulation of Asymmetric Spreading Rates

[8] The computation of the solution for a given model requires three preliminary steps: (1) the stream

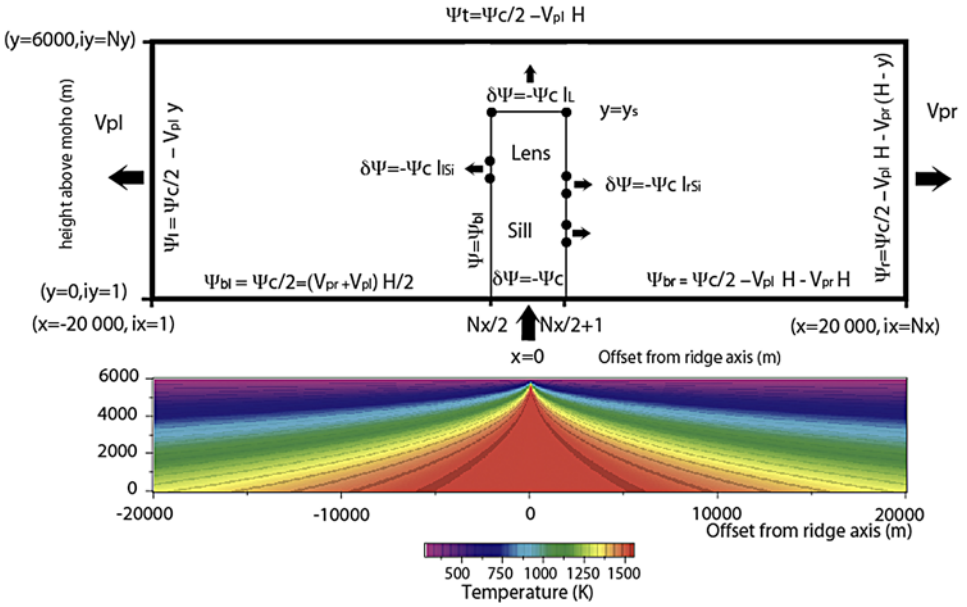

Figure 1. (top) Sketch of the stream function (Ψ) and temperature (T) internal and boundary conditions. The computation grid is composed of Nx horizontal columns (from 1 to Nx, x = −L to x = L) and Ny rows (from 1 to Ny, y = 0 to y = H). Nx must be even, in order to get the ridge axis location between the two adjacent middle columns (n = Nx/2 and n = (Nx/2) + 1). The Ψ boundary conditions impose the balance between the volume of crust flowing out through the lateral boundaries and the volume of magma injected at the ridge axis. At the Moho level, Ψ is constant (impervious boundary), except at the ridge axis, where the jump ($\Psi_{bl} - \Psi_{br}$) is equal to the lineic crustal discharge of the ridge Ψ_c (see text). At the lateral edges of the box, the Ψ boundary conditions are proportional to the y position. The style of magma intrusions is imposed by internal conditions at the ridge axis. The tip of a numerical needle delivers melt at the perched lens level, while its "laterally perforated" shaft discharges melt at chosen sill levels. (bottom) Initial and boundary conditions are also applied to the temperature field according to the half-space lithospheric cooling law, which takes into account, for both sides of the ridge, the asymmetric plate spreading (equation (14)).

function external boundary conditions and the initial and boundary temperature conditions are calculated from the values of the left and right spreading rates; then, (2) the style of magma intrusion is used to set internal, thermal and stream function conditions at the ridge axis (see section 6); and, finally, (3) a laminar flow is computed for the stream function and a half infinite cooling is computed for the temperature. The asymmetrical properties of the ridge (spreading rates, sill/lens distribution) are fully taken into account through these calculations. It is only after this initialization process ends that an iterative process starts by alternatively solving the temperature and the motion. This process continues until it reaches a stationary state.

[9] Figure 2 shows an example of the stream function (top) and related temperature field (bottom) obtained for asymmetric spreading rates. The left plate velocity is 9 cm a^{-1}, while the right is only 1 cm a^{-1}. The tightening of the streamlines for the left part is due to high flow rates, while the right side is sluggish. The strongly asymmetric final temperature field also reflects the stronger heat advection of the left plate.

6. Style of Melt Injection

[10] In order to simulate the detailed structure of magma intrusions, we applied internal conditions on the two central columns of the computational grid (Figure 1). An isothermal (1280°C) needle-like injection delivers melt to the ridge axis. The melt is injected at the needle hub (Moho) to the bevel (melt lens). Sill intrusions are simulated as holes at different levels of the needle shaft. The internal conditions are introduced as jumps in the stream function (following equations (15) and (16)) that simulate the discharge flowing through lateral holes of the needle shaft.

$$\sum_{n=0}^{n_{ls}} Ils_n + Il + \sum_{n=0}^{n_{rs}} Irs_n = 1 \qquad (15)$$

$$\delta\Psi ls_n = -\Psi_C \; Ils_n$$
$$\delta\Psi l = -\Psi_C \; Il$$
$$\delta\Psi rs_n = -\Psi_C \; Irs_n \qquad (16)$$

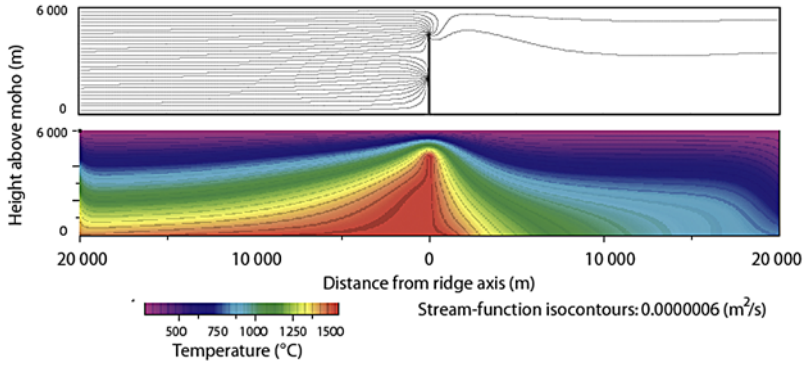

Figure 2. Stream function and temperature field obtained for an asymmetric spreading rate of (left) 9 cm a^{-1} and (right) 1 cm a^{-1}. Fifty percent of the melt is injected through the perched lens, while the remainder is injected through two left and right sills (25% each), symmetrically located at the ridge axis, 2000 m above the Moho. The thermal conductivity follows the crystallization (viscosity) according equation (17), with the hard phase conductivity twice that of the weak phase.

Figure 3 shows the stream function (top) and temperature field (bottom) obtained for a symmetrically spreading mid-ocean ridge, but with an asymmetric distribution of sills for the left and the right plates. The flow escaping the perched lens contributes to the accretion of both plates, which are respectively supplemented by the left and right sill discharges. Because heat is not advected symmetrically, the temperature field is asymmetric relative to the ridge axis, implying that thermal histories will be different for each plate.

7. Simulating the Transitions of Physical Properties

[11] As mentioned above, the conservation equations for our model take into account all the spatially variable terms for viscosity and thermal conductivity. This is an ambitious goal considering the sharp transitions observed in nature for these physical parameters. To avoid precision losses during finite differencing of the spatial derivatives, we use arctan-like, Γ step functions (equation (17)), which have analytical forms for their spatial derivatives. The threshold and sharpness of the transitions can be tuned easily with only two parameters.

[12] Thus crystallization induces a viscosity transition from a hot, weak phase viscosity, η_w, to a cold, strong phase viscosity, η_s. Considering the mathematical form of the Γ step function, 88% of the crystallization occurs over a temperature range ($2 \times \delta T$) centered on the medium crystallization temperature T_c.

$$\Gamma_c(T) = \frac{1}{2}\left(1 + \tanh\left(\frac{T - T_c}{\delta T}\right)\right) \tag{17}$$

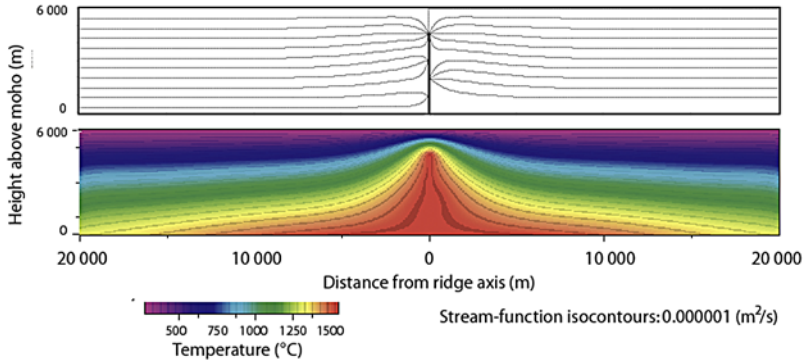

Figure 3. (top) Stream function and (bottom) temperature field obtained for a symmetrically spreading ridge (5.5 cm a^{-1}) with asymmetric left and right sill distributions. Two sills on the left side are located at 1000 and 3000 m above the Moho, respectively, while the right side has only one sill at 2000 m. The thermal conductivity follows the crystallization (viscosity) according to equation (17), with the hard phase conductivity twice that of the weak phase.

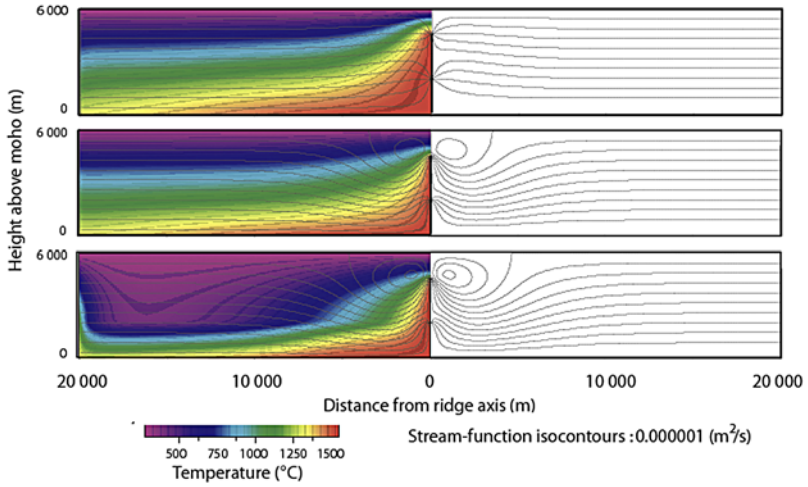

Figure 4. Evolution of the (left) thermal structure and the (right) stream function for a symmetric spreading rate of 5.5 cm a^{-1}. The magma is injected 50% through the perched lens 4500 m above the Moho and through two left and right sills (25% each) 2000 m above the Moho. (top) The hydrothermal cooling follows the crystallization (or the viscosity) with a hard phase thermal conductivity twice that of the weak phase (equation (17)). (middle) The ratio of the hard to weak thermal conductivity is 8. (bottom) The hydrothermal cooling transition depends on both the depth and the distance from the ridge through equation (19).

Following equation (17), the analytical expression for the viscosity variation and its spatial derivatives becomes equation (18).

$$\eta(T) = \eta_w \ \Gamma_c(T) + \eta_s(1 - \Gamma_c(T)) \tag{18}$$

Similar step functions simulate the spatial variations of the thermal conductivity, which makes variable functional forms of k(x, y) possible, based on viscosity (equation (19)), and/or depth, and/or offset from the ridge axis (equations (20) and (21)).

$$k(x,y) = k_m \ \Gamma_o + (k_h \ \Gamma_h + k_m(1 - \Gamma_h))(1 - \Gamma_o) \tag{19}$$

$$\Gamma_h(y) = \frac{1}{2}\left(1 + \tanh\left(\frac{y - y_h}{\delta y_h}\right)\right) \tag{20}$$

$$\Gamma_o(x) = \frac{1}{2}\left(1 + \tanh\left(\frac{x - x_o}{\delta x_o}\right)\right) for \ x > 0 \tag{21}$$

Figure 4 depicts the solution obtained at the end of the computation of a model with fully symmetric spreading rates and style of magma injection. So are the final stationary stream function (Figure 4, right) and temperature fields (Figure 4, left). The rows of Figure 4 correspond to different hydrothermal cooling patterns. The first is based on equation (17), with a thermal diffusivity transition following the crystallization (or the viscosity). The hard phase diffusivity is twice that of the weak phase. The second row corresponds to the same hydrothermal cooling dependency but with a higher contrast between the strong and weak phases. Finally, for the case displayed in the third row of Figure 4, the hydrothermal cooling depends both on the depth and on the offset from the ridge (equation (19)). This type of case is interesting because, if the hydrothermal cooling affects the temperature near the ridge, the cooled rocks are carried by advection of the crust far from the ridge axis, toward the lateral boundaries of the computation box. A detailed examination shows that, as soon as the hydrothermal cooling becomes negligible (far from the ridge following equations (19) and (21)), the temperature rises again with the diffusion of basal mantle heat flux, which slowly reheats the crustal temperature until it reaches the thermal half-space cooling lateral boundary conditions.

8. Numerical Resolution and Accuracy

[13] We solve the stream function and vorticity equations with Alternate Direction Implicit schemes, but we introduce the temperature advection with a half-implicit scheme [*Douglas and Rachford*, 1956]. Second-order accurate centered finite differences are used to calculate the first- and second-order derivatives on a regular grid in both the x and y directions.

[14] Applying internal conditions inside the box requires that the resolutions of the rows and columns be split into several segments. The numerical algorithm offers the possibility to split each column and row into several segments (up to five) bounded by external or internal conditions. After this segmentation, classical three-row matrix solvers operate

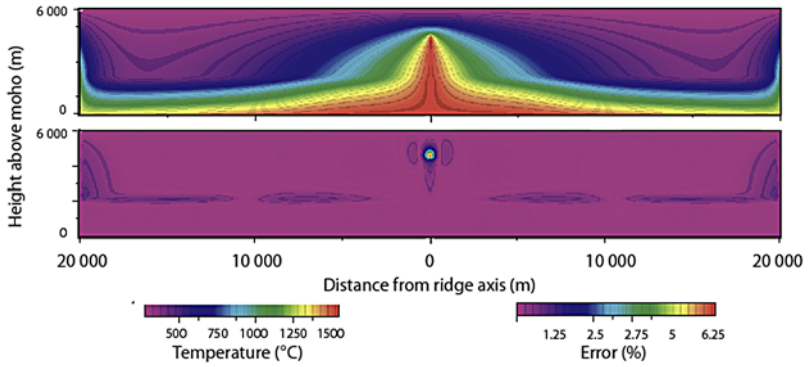

Figure 5. Comparison of the temperature fields obtained for left and right symmetric spreading rates of 5.5 cm a^{-1}. The magma is injected 50% through the perched lens 4500 m above the Moho and through two left and right sills (25% each) 2000 m above the Moho. The hydrothermal cooling depends on the depth and on the offset from the ridge axis. This case was computed with a G_1 (600 × 100 points) and a G_2 computation grid (1798 × 298 points). (top) The differences for the final temperature fields are not decipherable by the naked eye. (bottom) The error map, which represents the quantity $100 \times (T_{G2} - T_{G1})/T_{G2}$ calculated over all the common points of grids G_1 and G_2, shows that the error remains below 1% almost everywhere. The errors, which are more pronounced at the sill and lens locations, are due to thinning of the needle and of the perched lens, since they are defined over the two central adjacent column events with the G2 grid.

alternatively in the x and y directions. Then, the coupled equations for vorticity, stream function and temperature are solved iteratively until the maximum correction, in each point of the computation grid between two temperature fields, falls below 0.1 ppM.

[15] We used two grid resolutions for the cases presented in this paper. The first, G1, has 600 × 100 computation points in the x and y directions, while the second (G2) is obtained by intercalating, in the x and y directions, two more points between each point of the G1 grid. Thus, the points of the G1 grid also belong to the G2 grid, which is three times thinner in both directions. This property allows us to assess the accuracy of the computation by calculating, over the G1 points, the difference between the temperature fields obtained with the G1 and G2 grids. The final temperature field differences between the models are negligible, and the error map, which represents the quantity $100 \times (T_{G2} - T_{G1})/T_{G2}$ (Figure 5), shows that the errors remain less than 1%. The errors are more pronounced at the sill and lens locations because needle and perched lens thinning automatically occurs with the transition from the G1 to the G2 grid.

9. Code Functioning

[16] The present version is adapted to the modern drawing application but may need a few simple reorganizations for other graphic libraries. The benchmark cases given with the code allow for checking the compilation and execution of the source code (see text file in auxiliary material).[1]

[1]Auxiliary materials are available in the HTML. doi:10.1029/2008GL036964.

Acknowledgments

[17] This work benefited from specific funding of John Ludden (INSU/CNRS). This work was possible thanks to a sabbatical stay of P. Machetel at the University of Granada funded by the Spanish "Ministerio de Ciencia e Innovación (MICINN)" (SAB2006–0207) and a "Poste Rouge" position of C. J. Garrido at Géosciences Montpellier funded by CNRS. C. J. Garrido acknowledges the funding of the Spanish MICINN through research grants BTE2006–1489 and PCI2006-A9-0580 and the financial support of the "Junta de Andalucia" research group RNM-0131.

References

Boudier, F., and A. Nicolas (1995), Nature of the Moho transition zone in the Oman ophiolite, *J. Petrol.*, *36*(3), 777–796.

Boudier, F., et al. (1996), Magma chambers in the Oman ophiolite: Fed from the top and the bottom, *Earth Planet. Sci. Lett.*, *144*(1–2), 239–250, doi:10.1016/0012-821X(96)00167-7.

Chen, Y. J. (2001), Thermal effects of gabbro accretion from a deeper second melt lens at the fast spreading East Pacific Rise, *J. Geophys. Res.*, *106*(B5), 8581–8588, doi:10.1029/2000JB900420.

Chen, Y. J., and J. Phipps Morgan (1996), The effects of spreading rate, the magma budget, and the geometry of magma emplacement on the axial heat flux at mid-ocean ridges, *J. Geophys. Res.*, *101*(B5), 11,475–11,482, doi:10.1029/96JB00330.

Chenevez, J., et al. (1998), Numerical models of magma chambers in the Oman ophiolite, *J. Geophys. Res.*, *103*(B7), 15,443–15,455, doi:10.1029/98JB00597.

Cherkaoui, A. S. M., W. S. D. Wilcock, R. A. Dunn, and D. R. Toomey (2003), A numerical model of hydrothermal cooling and crustal accretion at a fast spreading mid-ocean ridge,

Geochem. Geophys. Geosyst., *4*(9), 8616, doi:10.1029/2001GC000215.

Coogan, L. A., et al. (2002), Constraining the cooling rate of the lower oceanic crust: A new approach applied to the Oman ophiolite, *Earth Planet. Sci. Lett.*, *199*(1–2), 127–146, doi:10.1016/S0012-821X(02)00554-X.

Coogan, L. A., G. R. T. Jenkin, and R. N. Wilson (2007), Contrasting cooling rates in the lower oceanic crust at fast- and slow-spreading ridges revealed by geospeedometry, *J. Petrol*, *48*(11), 2211–2231.

Crawford, W. C., and S. C. Webb (2002), Variations in the distribution of magma in the lower crust and at the Moho beneath the East Pacific Rise at 9 degrees–10 degrees N, *Earth Planet. Sci. Lett.*, *203*(1), 117–130, doi:10.1016/S0012-821X(02)00831-2.

Deschamps, A., and T. Fujiwara (2003), Asymmetric accretion along the slow-spreading Mariana Ridge, *Geochem. Geophys. Geosyst.*, *4*(10), 8622, doi:10.1029/2003GC000537.

Douglas, J., and H. H. Rachford (1956), On the numerical solution of heat conduction problems in two and three space variables, *Trans. Am. Math. Soc.*, *82*, 409–412, doi:10.2307/1993056.

Dunn, R. A., et al. (2000), Three-dimensional seismic structure and physical properties of the crust and shallow mantle beneath the East Pacific Rise at 9 degrees 30′N, *J. Geophys. Res.*, *105*(B10), 23,537–23,555, doi:10.1029/2000JB900210.

Garmany, J. (1989), Accumulations of melt at the base of young oceanic-crust, *Nature*, *340*(6235), 628–632, doi:10.1038/340628a0.

Garrido, C. J., et al. (2001), Variation of cooling rate with depth in lower crust formed at an oceanic spreading ridge: Plagioclase crystal size distributions in gabbros from the Oman ophiolite, *Geochem. Geophys. Geosyst.*, *2*(10), 1041, doi:10.1029/2000GC000136.

Kelemen, P. B., et al. (1997), Geochemistry of gabbro sills in the crust-mantle transition zone of the Oman ophiolite: Implications for the origin of the oceanic lower crust, *Earth Planet. Sci. Lett.*, *146*(3–4), 475–488, doi:10.1016/S0012-821X(96)00235-X.

Maclennan, J., et al. (2004), Thermal models of oceanic crustal accretion: Linking geophysical, geological and petrological observations, *Geochem. Geophys. Geosyst.*, *5*, Q02F25, doi:10.1029/2003GC000605.

Maclennan, J., et al. (2005), Cooling of the lower oceanic crust, *Geology*, *33*(5), 357–360, doi:10.1130/G21207.1.

Morton, J. L., and N. H. Sleep (1985), A mid-ocean ridge thermal model - constraints on the volume of axial hydrothermal heat flux, *J. Geophys. Res.*, *90*, 11,345–11,353, doi:10.1029/JB090iB13p11345.

Nedimovic, M. R., et al. (2005), Frozen magma lenses below the oceanic crust, *Nature*, *436*(7054), 1149–1152, doi:10.1038/nature03944.

Phipps Morgan, J., and Y. J. Chen (1993), The genesis of oceanic-crust-magma injection, hydrothermal circulation, and crustal flow, *J. Geophys. Res.*, *98*(B4), 6283–6297, doi:10.1029/92JB02650.

Sleep, N. H. (1975), Formation of oceanic crust - some thermal constraints, *J. Geophys. Res.*, *80*(29), 4037–4042, doi:10.1029/JB080i029p04037.